Xiangmeng Meng, Antoni Artinov, Marcel Bachmann, Michael Rethmeier

Numerical and experimental investigation of thermo-fluid flow and element transport in electromagnetic stirring enhanced wire feed laser beam welding

WISSEN IM ZENTRUM
UNIVERSITÄTSBIBLIOTHEK

Technische
Universität
Berlin

Numerical and experimental investigation of thermo-fluid flow and element transport in electromagnetic stirring enhanced wire feed laser beam welding

Xiangmeng Meng[a,*], Antoni Artinov[a], Marcel Bachmann[a], Michael Rethmeier[a,b]

[a] BAM Federal Institute for Materials Research and Testing, Unter den Eichen 87, 12205 Berlin, Germany

[b] Technical University Berlin, Institute of Machine Tools and Factory Management, Pascalstraße 8-9, 10587 Berlin, Germany

Corresponding author: xiangmeng.meng@bam.de

Abstract

The introduction of electromagnetic stirring to laser beam welding can bring several beneficial effects e.g. element homogenization and grain refinement. However, the underlying physics has not been fully explored due to the absence of quantitative data of heat and mass transfer in the molten pool. In this paper, the influence of electromagnetic stirring on the thermo-fluid flow and element transport in the wire feed laser beam welding is studied numerically and experimentally. A three-dimensional transient heat transfer and fluid flow model coupled with dynamic keyhole, magnetic induction and element transport is developed for the first time. The results suggest that the Lorentz force produced by an oscillating magnetic field and its induced eddy current shows an important influence on the thermo-fluid flow and the keyhole stability. The melt flow velocity is increased by the electromagnetic stirring at the rear and lower regions of molten pool. The keyhole collapses more frequently at the upper part. The additional elements from the filler wire are significantly homogenized because of the enhanced forward and downward flow. The model is well verified by fusion line shape, high-speed images of molten pool and measured element distribution. This work provides a deeper understanding of the transport phenomena in the laser beam welding with magnetic field.

Keywords: thermo-fluid flow; element transport; laser beam welding; magnetohydrodynamics; numerical analysis

1. Introduction

The deep penetration laser beam welding (LBW) has developed to one of the most promising metal joining methods in the modern manufacturing industry. However, typical autogenous LBW may also confront some issues, including high sensitivity to gap tolerance and severe loss of alloying element due to metal evaporation [1]. It has been found that better capacity of gap bridging and improvement of metallurgical properties can be achieved by LBW with filler wire, namely wire feed

LBW (WFLBW) [2]. However, the molten pool of LBW experiences an extremely high cooling rate (order of magnitude about $10^5 \sim 10^6$ K/s), and there is usually no sufficient time for the downward transfer of additional element to the root of the final weld, especially for thick plate welding. The additional element concentrates at the upper part of the weld, resulting in deterioration of the homogeneity of the weld property.

The contactless electromagnetic technique is a commonly used way to control the fluid flow during material melting process [3,4]. Based on the magnetohydrodynamics (MHD) theory, a current density $\vec{j}$ will be induced when electrically conducting fluid, for example liquid metal, flowing in a magnetic field, which gives

$$\vec{j} = \sigma_{e}\left(\vec{v}\times\vec{B}+\vec{E}\right) \quad (1)$$

where σ_e, $\vec{v}$, $\vec{B}$ and $\vec{E}$ are electrical conductivity, flow velocity, magnetic flux density and induced electric field, respectively. The external magnetic field and its induced current produce a volumetric Lorentz force $\vec{F}_L$:

$$\vec{F}_L = \vec{j}\times\vec{B} \quad (2)$$

It has two components: one resulting from temporal variation of magnetic field ($\vec{E}$) and one resulting from $\vec{v}\times\vec{B}$ term in Eq. (1), which is always opposite to the flowing direction, namely, magnetic braking. Different effects such as stirring, supporting or deceleration can be produced to control the thermo-fluid flow by choosing a proper external magnetic field. Therefore, it is considered as a potential way to overcome the issues occurring in WFLBW.

Kern et al. first attempted to apply external magnetic field to high-speed LBW and found that the humping defect was suppressed [5]. When introducing a steady magnetic field to the LBW process, the weld bead tends to change from a wineglass shape to a cone shape, which benefits a more uniform mechanical stress distribution inside the weld specimen [6, 7]. Avilov et al. suggested that oscillating magnetic field provided an effective support against the metallostatic pressure in full penetration LBW, and suppressed the root sagging [8]. Fritzsche et al. employed a transverse oscillating magnetic field with high frequency (2 kHz~10 kHz) in partial penetration LBW of Al, by which the process porosity was dramatically reduced, and the surface of the weld bead was smoothed [9]. Low-frequency coaxial alternating magnetic field within 25 Hz was used to produce electromagnetic stirring (EMS) in the molten pool of WFLBW and homogeneous dilution of Si element from the filler wire in Al molten pool was achieved to prevent the hot cracking defect [10].

The heat and mass transfer behaviors in the molten pool play an underlying role on determining the weld geometry and the element distribution. Researchers have proposed several

experimental approaches to reveal the melt flow in LBW with magnetic field, such as microfocused X-ray transmission [11] and high-speed imaging through metal/glass sandwich [12]. However, due to the extremely bright plasma, high temperature and velocity gradients in molten pool as well as the non-transparency of the liquid metal, the experimental measurement of the transient and spatial evolution of the molten pool in LBW is still very limited.

With the development of computational capacity, some multi-physical modelling works of LBW with magnetic field have been conducted to describe the heat and mass transfer phenomena. Bachmann et al. developed a steady-state 3D numerical model of LBW with magnetic field. The thermo-fluid dynamics in the molten pool under different magnetic field patterns (steady or oscillating), penetration states (partial or full penetration) and material types (ferromagnetic or non-ferromagnetic) were calculated and analyzed [13-17]. Numerical analysis was performed to investigate the thermoelectric currents and thermoelectric-magnetic effects in full penetration LBW of aluminum with a steady magnetic support [18]. The influence of the low-frequency coaxial magnetic field on the melt flow and the element distribution in WFLBW was studied numerically by Gatzen et al [19]. It was found that the induced EMS influenced the melt flow pattern significantly, and therefore changed the element distribution. However, a fixed keyhole whose boundary was set as the boiling temperature of the material was used in these models for simplification. The keyhole dynamics which had considerable impact on the thermo-fluid flow were not taken into consideration. Recently, Chen et al. studied the thermoelectric effect on the weld microstructure of LBW with steady magnetic field using a fuller numerical model considering the keyhole dynamics [20].

A critical review of the literature shows that a deep understanding of the thermo-fluid flow in LBW with a magnetic field is still not available. Moreover, the direct role of the thermo-fluid flow on determining the final element distribution has not been discussed quantitatively either. Here a numerical and experimental research of the EMS enhanced WFLBW (EMS-WFLBW) is reported, in which an external oscillating magnetic field is applied to produce EMS in the molten pool. A three-dimensional transient heat transfer and fluid flow model coupled with free surface tracking, magnetic induction and element transport is developed to calculate the MHD behavior (eddy current, Lorentz force etc.) as well as the temperature and velocity profiles, the keyhole dynamics and the element distribution. The model is well tested against experimental results. The influence of EMS on the heat and mass transfer in the molten pool is analyzed and discussed. The element distribution associated with the thermo-fluid flow is rationalized using numerical data and results from energy dispersive X-ray spectroscopy (EDX) analysis.

2. Mathematical modelling

Since the physics in keyhole LBW and the interaction between the magnetic field and the materials (vapor, liquid and solid) are very complex, it is a formidable task to incorporate all the physical factors into a mathematical model. To make the model tractable, several simplifications are made in current study, which are given below:

(i) The liquid metal is Newtonian and incompressible, and the flow in molten pool is laminar. Boussinesq approximation is employed to treat the buoyancy term [21].

(ii) The base metal maintains completely non-ferromagnetic during welding, which means no transformation from austenite to ferrite occurs [15].

(iii) The vapor plume is weakly ionized during fiber laser welding, so the gaseous phase in the model is considered as non-conductive [22].

(iv) The thermoelectric effect and the Joule heating are not taken into consideration. The influence of the magnetic field on the filler material transfer is neglected.

2.1 Governing equations

The heat transfer, fluid flow, free surface profile, element distribution and MHD behavior can be obtained by solving mass conservation, Navier-Stokes, energy, volume-of-fluid (VOF), element transport and magnetic induction equations. Under the above assumptions, the governing equations in a fixed Cartesian coordinate are written as follows:

- Mass conservation equation

$$\nabla \cdot \vec{v} = \frac{m_w}{\rho} \quad (3)$$

where ρ is the material density and m_w is the mass source from filler wire.

- Navier-Stokes equation

$$\rho \left(\frac{\partial \vec{v}}{\partial t} + \vec{v} \cdot \nabla \vec{v} \right) = -\nabla p + \mu \nabla^2 \vec{v} - \beta \rho (T - T_L) \vec{g} + \rho \vec{g} - \mu K \vec{v} + m_w \vec{v}_w + \vec{S}_m \quad (4)$$

where t is the time, p is the pressure, μ is the dynamic viscosity, β is the thermal expansion coefficient, $\vec{g}$ is the vector of gravity acceleration, T is the temperature, T_L is the liquids temperature, $\vec{v}_w$ is the velocity vector of the filler material in the liquid bridge and $\vec{S}_m$ is the additional momentum source. K is the Carman–Kozeny equation coefficient which is a function of liquid fraction [23]:

$$K = C \frac{(1 - f_L)^2}{f_L^3 + \delta} \quad (5)$$

where C is the mushy zone parameter, δ is a small number with an order of magnitude of 1×10^{-6} for numerical convergence. The dependency of the liquid fraction f_L on temperature is assumed to be linear.

$$f_L = \begin{cases} 0 & (T \leq T_S) \\ \dfrac{T - T_S}{T_L - T_S} & (T_S < T < T_L) \\ 1 & (T \geq T_L) \end{cases} \quad (6)$$

where T_S is the solidus liquids temperature.

- Energy equation

$$\rho \left[\frac{\partial h}{\partial t} + (\vec{v} \cdot \nabla) h \right] = \nabla \cdot (k \nabla T) + h_w + S_q \quad (7)$$

$$h = \int c_p(T) dT + f_L \Delta L_m \quad (8)$$

Here k is the thermal conductivity, h is the enthalpy, h_w is the energy source from the liquid filler material, S_q is the additional energy source term, c_p is the specific heat and ΔL_m is the melting latent heat.

- VOF equation

$$\frac{\partial \phi}{\partial t} + \nabla \cdot (\vec{v} \phi) = \phi_w \quad (9)$$

where ϕ is the volume fraction and ϕ_w is the volume source from the filler material.

- Element transport equation

$$\frac{\partial \phi_{steel} \rho_{steel} C}{\partial t} + \nabla \cdot \left(\phi_{steel} \rho_{steel} \vec{v} C - \phi_{steel} D \nabla C \right) = C_w \quad (10)$$

where C is the weight percentage, ϕ_{steel} is the volume fraction of the steel, D is the element diffusion coefficient in iron and C_w is the element source from the filler wire.

- Magnetic induction equation

From Ohm's law and Maxwell's equation, the magnetic induction equation which provides the coupling between the flow field and the magnetic field can be written as:

$$\frac{\partial \vec{b}}{\partial t} + (\vec{v} \cdot \nabla) \vec{b} = \frac{1}{\mu_m \sigma_e} \nabla^2 \vec{b} + \left((\vec{B}_0 + \vec{b}) \cdot \nabla \right) \vec{v} - (\vec{v} \cdot \nabla) \vec{B}_0 \quad (11)$$

where μ_m is the magnetic permeability, $\vec{B}_0$ is the externally imposed oscillating magnetic field which is taken from a cold metal measurement and $\vec{b}$ is the secondarily induced magnetic field from the

temporal variation of $\vec{B}_0$ and the liquid flow. Fig. 1 shows the distribution of the normalized external magnetic flux density along the x-z central plane.
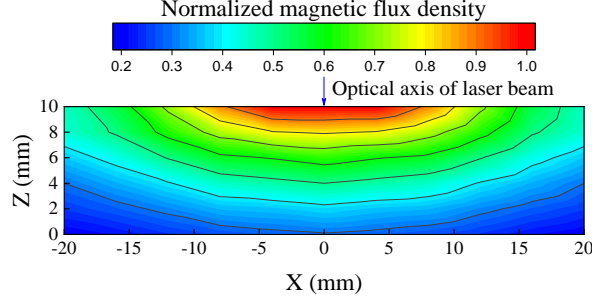

Fig. 1 Normalized magnetic flux density from cold metal measurement.

The induced current density is calculated as:

$$\vec{j} = \frac{1}{\mu_m} \nabla \times \left(\vec{B}_0 + \vec{b} \right) \quad (12)$$

The Lorentz force can be determined by Eq. (2) and is implemented into the momentum source term $\vec{S}_m$ in Eq. (4).

2.2 Physical models in WFLBW

2.2.1 Heat source model

The allocation of the laser energy in the WFLBW is more complex than that in the autogenous LBW. It determines both the transfer mode of filler material and the thermal behavior of molten pool. Part of the laser spot first irradiates on the surface of the filler wire to form a liquid front, meanwhile, some energy is dissipated into the atmosphere due to the reflection. The rest of the laser energy heats, melts and evaporates the base metal to form the molten pool and the keyhole. Most of it is absorbed at the keyhole wall under multiple reflections, but a small amount of the energy is still lost by reflection and vaporization. Hence, four coefficients are needed to describe the energy allocation, including the absorption ratio at the wire liquid front η_w, the dissipation ratio from the filler wire η_{wloss}, the absorption ratio at the keyhole wall η_k and the dissipation ratio from the keyhole wall η_{kloss}.

High-speed imaging was conducted using a Photron FASTCAM SA4 camera to develop an intuitive understanding of the interaction between laser beam, filler wire and molten pool, as shown in Fig. 2. The principal optical axis of the camera was perpendicular to the welding direction and had a 10° respect to the welding plane. The capture frequency was 500 frames per second. The high-speed images show that a liquid bridge transfer occurs, which is favorable to a stable welding process.
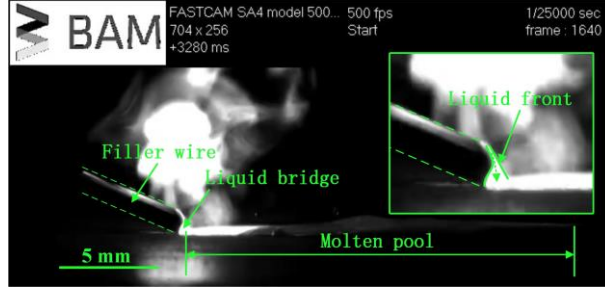
Fig. 2 High-speed images of molten pool and filler material transfer

The average temperature of the liquid bridge T_w is assumed to be 2900 K in this paper [24], and the absorption ratio at the wire liquid front η_w can be calculated as:

$$\eta_w = \frac{\pi v_{feed} \rho_w r_w^2 \left[c_{pw}\left(T_w - T_0\right) + \Delta H_w \right]}{P_L} \approx 7.2\% \quad (13)$$

where P_L is the laser power, v_{feed} is the wire feeding speed, ρ_w, r_w and c_{pw} are the density, radius and specific heat of the filler wire, respectively.

The laser reflectivity R at the wire liquid front is calculated based on the Hagen–Rubens relationship [25].

$$R = \frac{1}{2}\left(\frac{1+\left(1-\varepsilon\cos\varphi\right)^2}{1+\left(1+\varepsilon\cos\varphi\right)^2} + \frac{\varepsilon^2 - 2\varepsilon\cos\varphi + 2\cos^2\varphi}{\varepsilon^2 + 2\varepsilon\cos\varphi + 2\cos^2\varphi} \right) \approx 0.69 \quad (14)$$

where ε is a laser- and material-dependent variable whose value is adapted to 0.25 in this study [26], φ is the incident angle of the laser beam on the wire liquid front which can be measured from the high-speed images.

The dissipation ratio from the filler wire η_{wloss} can be calculated as:

$$\eta_{wloss} = \frac{R}{1-R}\eta_w \approx 15.8\% \quad (15)$$

The thermal efficiency of the laser entering the keyhole can reach up to 85% [27], so the absorption ratio at the keyhole wall η_k is calculated as

$$\eta_k = 0.85 \times \left(1 - \eta_w - \eta_{wloss}\right) \approx 65\% \quad (16)$$

A rotary Gauss volumetric heat source is used in the model to represent the spatial distribution of the laser energy in the keyhole [28]:

$$q_L = \frac{9\eta_k P_L}{\pi R_0^2 H(1-e^{-3})} \exp\left[\frac{-9r^2}{R_0^2 \ln\left(\dfrac{H}{z}\right)} \right] \quad (17)$$

in which $r^2 = \left(x - v_{\text{speed}}t\right)^2 + y^2$, v_{speed} is the welding speed, R_0 is the distribution radius of the heat source and H is the time-dependent keyhole depth.

In addition, the secondary heating effect from the high-temperature plume and the latent heat release from the metal vapor's re-condensation are also considered using the model from Muhammad et al [29].

2.2.2 Forces on keyhole wall

The recoil pressure due to evaporation is described as follows [30]:

$$p_r = \frac{AB}{\sqrt{T}} \exp\left(-\frac{m_a \Delta L_v}{N_a k_b T}\right) \quad (18)$$

where p_r is the recoil pressure, A and B are two evaporation coefficients, m_a is the molar mass, ΔL_v is the evaporation latent heat, N_a is the Avogadro constant and k_b is the Boltzmann constant. For pure iron, A is equal to 0.55 and B is equal to 3.9×10^{12} kg/m·s^2.

The temperature-dependent surface tension coefficient is calculated as:

$$\gamma = \gamma_0 - A_T(T - T_L) - R_g T \Gamma_s \ln(1 + K_s a_s) \quad (19)$$

$$K_s = k_l \exp\left(\frac{-\Delta H_0}{R_g T}\right) \quad (20)$$

where γ_0 is the surface tension of iron at the melting point, A_T is the surface tension gradient, R_g is the gas constant, Γ_s is the surface excess at saturation, a_s is the sulfur activity, k_l is the entropy factor and ΔH_0 is the heat of absorption.

The normal capillary pressure p_{ca} and the tangential Marangoni stress τ_{ma} can be written as:

$$p_{\text{ca}} = \gamma \kappa \quad (21)$$

$$\tau_{\text{ma}} = \frac{\partial \gamma}{\partial T} \frac{\partial T}{\partial \vec{s}} \quad (22)$$

where κ and $\vec{s}$ are the curvature and the tangential vector of keyhole surface, respectively.

A simplified method developed by Cho et al. for the stagnation pressure and the shear stress from the high-speed metal vapor are used [26]. It is assumed that the velocity of the metal vapor increases linearly from the bottom of the keyhole to the entrance of the keyhole.

2.3 Computational domain and boundary conditions

Fig. 3 shows the schematic of the computational domain. The dimensions of the geometric model are 30 mm × 8 mm × 12 mm, in which a 2 mm thick gas phase layer is built above the workpiece for the implementation of the VOF method. The melting procedure of the filler wire is not

considered in the model. A moving inlet of filler material which has the temperature and radius of the liquid bridge is set at the top of the model. The central zone of the computational domain (-2.5 mm ≤ y ≤ 2.5 mm) is finely meshed with hexahedral cells with uniform dimension of 0.2 mm. The cell size expends gradually from 0.2 mm to 1 mm at the rest part of the computational domain. 271,260 control volumes are generated. The mesh density has been confirmed to be sufficiently accurate in the previous studies [26, 31].
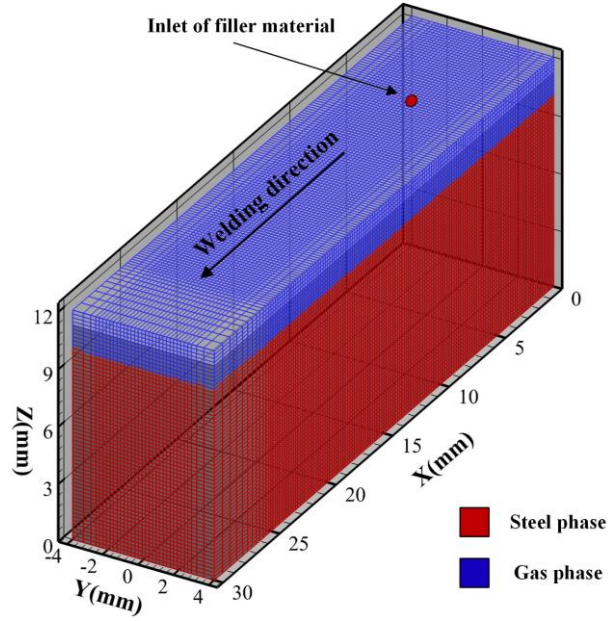

Fig. 3 Schematic of computational domain.

The energy balance on the keyhole wall is given as

$$k\frac{\partial T}{\partial \vec{n}} = q_L - h_c(T-T_0) - \sigma\varepsilon_r(T^4-T_0^4) - \rho v_{evp}\Delta L_v + q_{plume} + q_{recond} \quad (23)$$

in which $\vec{n}$ is the normal vector of the free surface, q_L is the laser energy density, h_c is the coefficient of convective heat transfer, σ is the Stefan-Boltzmann constant and ε_r is the emissivity. v_{evp} is the evaporation recession speed of the free surface, which can be determined by considering the velocity jump across the Knudsen layer [32], q_{plume} is the secondary heating effect from the high-temperature plume, q_{recond} is the latent heat release from the metal vapor's re-condensation.

The force balance on the keyhole wall in normal and tangential direction can be written as

$$-p + 2\mu\frac{\partial v_n}{\partial \vec{n}} = -p_r - p_{vapor} + p_{ca} \quad (24)$$

$$-\mu\frac{\partial v_t}{\partial \vec{n}} = \tau_{ma} + \tau_{vapor} \quad (25)$$

where p_{vapor} is the stagnation pressure and τ_{vapor} the shear stress from the high-speed metal vapor. v_n and v_t are the normal velocity and the tangential velocity.

The remaining energy, momentum and electromagnetic boundary conditions are given in Table 1. The initial conditions are

$$T\big|_{t=0} = 300\,\text{K}, \ \vec{v}\big|_{t=0} = 0, \ \vec{b}\big|_{t=0} = 0 \quad (26)$$

Table 1 Energy, momentum and electromagnetic boundary conditions

	Energy	Momentum	Electromagnetic
Top	$T_w = 2900$ K if $r \leq 0.3$ mm	$v_w = 0.14$ m/s if $r \leq 0.3$ mm	$\vec{j} = 0$
Side steel surface	Continuum boundary [33]	$\vec{v}=0$	Continuum boundary [33]
Side gas surface	$\partial T / \partial \vec{n} = 0$	$p = p_a$	$\vec{j} = 0$
Bottom	$k\,\partial T / \partial n = -h_c(T - T_0) - \sigma \varepsilon_r (T^4 - T_0^4)$	$\vec{v}=0$	$\vec{j} = 0$

p_a is the ambient pressure.

2.4 Numerical consideration

The commercial software ANSYS Fluent is used to solve the transport equations and the VOF equation. The second order upwind method is used for the spatial discretization of energy, momentum, magnetic field and element content scalar. The PISO algorithm is applied for the velocity-pressure coupling. About sixty hours of computational time are needed to simulate around 0.9 s real-time welding using a high performance computing cluster.

A base material of AISI 304 austenitic steel and a filler wire of nickel-based Inconel 625 alloy are used. Considering the significant difference of Ni content between the base metal and the filler material (10% vs. 58%), the Ni was chosen as the marking element to characterize the mixing in the molten pool in both experiment and simulation. The thermophysical properties are listed in Fig. 4 and Table 2. The surface tension gradient due to the difference of chemical composition is ignored in the current study. All the metal properties in the equations are percentage-weighted averages of the base metal and the filler material.

Table 2 Thermophysical properties of materials [36-38].

Properties	304 steel	Inconel 625 alloy
Density (kg/m^3)	6900	8440
Thermal conductivity (W/m·K)	In Fig. 4	In Fig. 4
Specific heat (J/kg·K)	In Fig. 4	575
Viscosity (Pa·s)	In Fig. 4	In Fig. 4
Surface tension coefficient (N/m)	In Fig. 4	-
Melting latent heat (kJ/kg)	274	227
Liquidus temperature (K)	1727	1623
Solidus temperature (K)	1673	1563
Emissivity	0.4	0.4
Expansion coefficient (/K)	1.2×10^{-5}	1.6×10^{-5}
Electric conductivity (S/m)	In Fig. 4	7.46×10^5
Magnetic permeability (H/m)	1.26×10^{-6}	1.26×10^{-6}
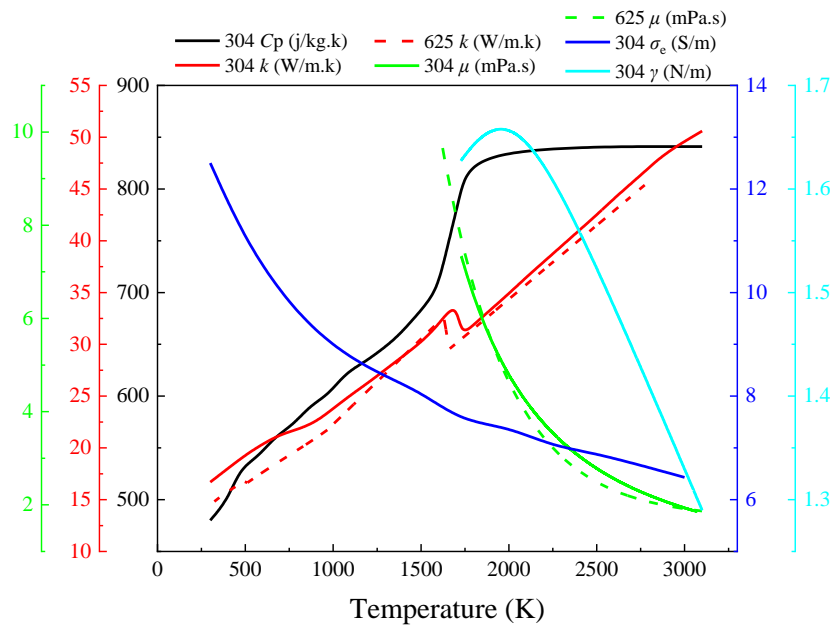
Fig. 4 Temperature dependent material properties

3. Experimental procedure

The dimension of the workpiece is 200 mm × 60 mm × 10 mm, and the diameter of the filler wire is 1.2 mm. An IPG YLR 20000 fiber laser system was used as laser source. Butt configuration with zero gap was performed, and the laser optical axis was perpendicular to the workpiece. The filler wire was fed in front of the laser spot with a 33° angle with respect to the workpiece, and the shielding gas of pure Argon was provided behind the laser spot. The alternating current electromagnet was mounted 2 mm above the workpiece and had a 75° angle with respect to the welding direction, as shown in Fig. 5. The gap between the two magnet poles was 20 mm and the cross-section of the magnet pole was 16 mm × 16 mm. The laser optic and the electromagnet system were fixed, and the welding speed was realized by moving the base metal during the experiment. The detailed welding
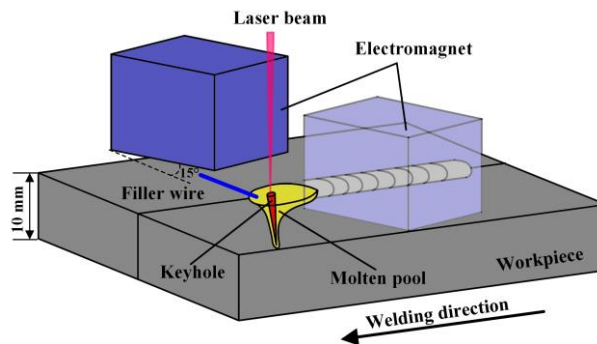
parameters can be found in Table 3.

Fig. 5 Experimental setup of EMS-WFLBW

Table 3 Process parameters used in the investigation

Laser power	7.5 kW
Laser spot diameter	0.52 mm
Wavelength	1070 nm
Focal length	350 mm
Focal position	-3 mm
Welding speed	1.3 m/min
Wire feeding speed	2.1 m/min
Shielding gas	20 l/min
Magnetic field frequency	3600 Hz
Magnetic field magnitude	235 mT

The macro-observation on the cross-section of the weld was performed by an optical microscope. The specimen was first prepared by mechanical grinding and polishing, and then etched by V2A etchant (100 ml H_2O, 100 ml HNO_3 and 10 ml HCl) at a temperature of 50 ℃ for 30 seconds. The distribution of Ni at the cross-section of the welded specimen was measured by EDX mapping. An additional EDX line analysis with higher resolution was performed to detect the Ni content along the center line.

4. Results and discussion

4.1 Verification of numerical model

The calculated fusion zone profiles are compared with the experimental ones in Fig. 6. The penetration depth is 8.1 mm for the WFLBW, while it decreases to 7.0 mm under the EMS. The numerical fusion lines for both processes agree well with the experimental results, proving the reasonability of the numerical model. The minor discrepancies between the calculated and experimental fusion lines are considered to come from: (1) using volumetric heat source to represent the spatial laser energy distribution and (2) tolerance range of the experimental fusion line. There is a certain deviation in the contour line of reinforcement for the EMS-WFLBW. It can be explained that the experimental weld bead surface is fluctuated to some extent, which cannot be reproduced by the current model.
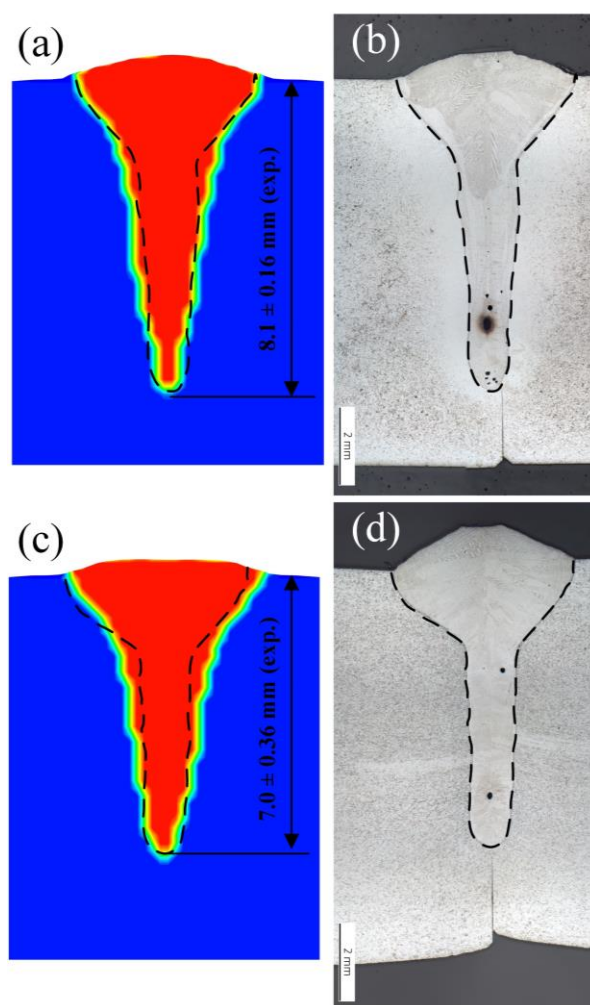
Fig. 6 Comparison of calculated and experimental fusion zones: (a) and (b) WFLBW, (c) and (d) EMS-WFLBW.

4.2 MHD behaviors and thermo-fluid flow

Fig. 7 shows the three-dimensional distribution of the induced current density in the workpiece. Since the electric conductivity of 304 stainless steel decreases with the temperature rising and the vapor in the keyhole is assumed as completely non-conductive, the high-temperature keyhole region acts as an electric barrier in the model. There are two nearly separated circulating currents with maximum value in magnitude of 1×10^7 A/m^2. The direction of the current can be either clockwise or counter-clockwise depending on the phase of the magnetic field. The current density in the molten pool is more irregular and complex compared to that in the solid metal because it is determined by the temporal variation of the magnetic field, the motion of the liquid metal as well as the temperature-dependent electric conductivity. In addition, the current concentrates on the upper and bottom region of the workpiece due to the skin effect.
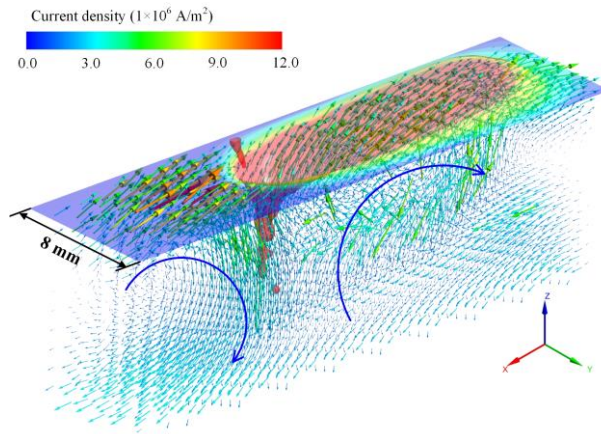

Fig. 7 3D distribution of the current density in workpiece ($t = 0.670$ s)

A volumetric Lorentz force is produced from the magnetic field and its induced electric current. It becomes outward and inward alternatively with a high frequency of 7200 Hz which is twice of the magnetic field frequency, as shown in Fig. 8(a) and (b). The maximum value lies in the range of $1.6\sim1.9 \times10^6$ N/m^3. The relative significance of the magnetic braking to the viscous force can be evaluated by a dimensionless Hartmann number (Ha), as given below:

$$Ha = B_{rms}\left(x, y, z\right)D_p\sqrt{\frac{\sigma}{\mu}} \quad (27)$$

where B_{rms} is the root mean square value of the magnetic flux density and D_p is the penetration depth which is chosen as the characteristic length scale. The maximum Hartmann number in the molten pool is about 7.5. It is suggested that the magnetic braking only shows minor influence on the fluid flow.

The Lorentz force is much stronger at the top region under the inhomogeneous magnetic field. Its gradient will enhance the stirring in the molten pool. The time-dependent Lorentz force at point P in Fig. 8(a) is plotted in Fig. 8(c). A sinusoidal form can be identified, and the downward force is typically stronger than the upward one. The time-averaged Lorentz force at point P is downward and has an order of magnitude of 10^5 N/m^3, which is coincident with numerical data from the literature [15]. It leads to a beneficial effect on the downward transport of additional elements from the filler wire.
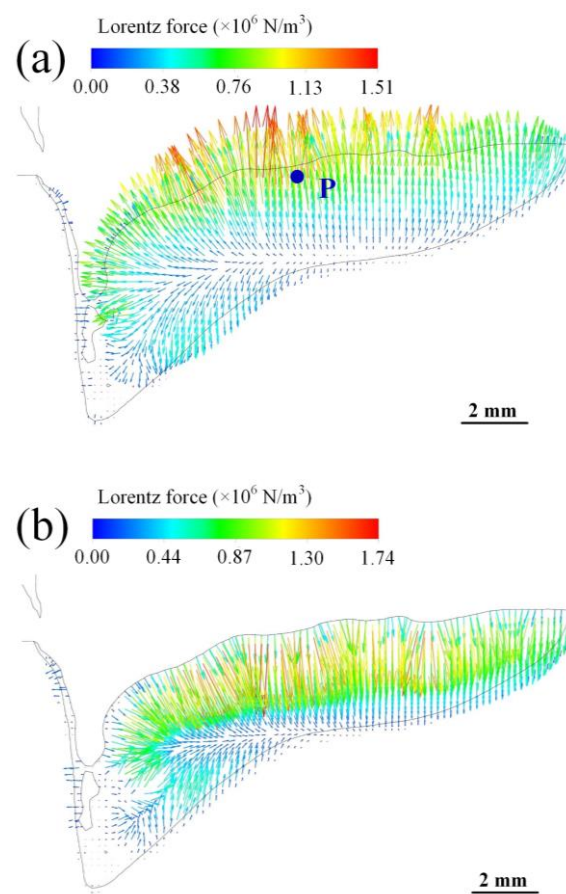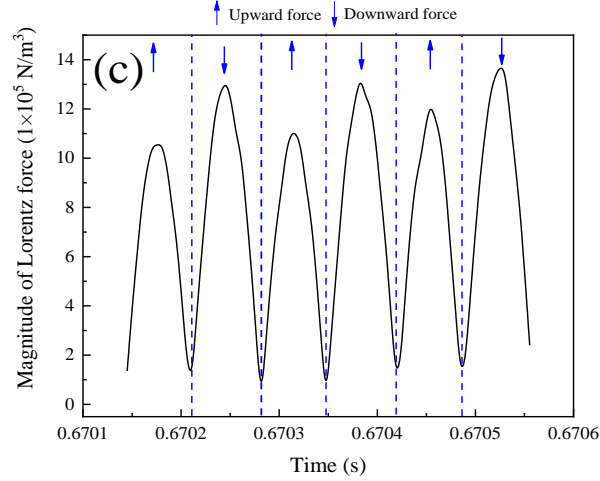
Fig. 8 Distribution of the Lorentz force in the molten pool: (a) t_0 (b) $t_0+1/4\times$magnetic field period, (c) time-dependent Lorentz force at Point P.

The temperature profile and the velocity field of the WFLBW and the EMS-WFLBW processes are shown in Fig. 9 and Fig. 10, respectively. The black line represents the solidus boundary. Fig. 9(a) shows a narrow and deep keyhole formed under the recoil pressure and a thin liquid layer on the keyhole front wall. The upper part of the molten pool is extended up to 20 mm which has a good agreement with the high-speed images (19.6 mm). The lower part is much shorter. The liquid metal first flows around the keyhole, and continues to flow backward along the lateral side of the molten pool. Thereafter the liquid metal changes its direction at the middle part, and flows forward along the x-z plane. The dominant flowing routine of the liquid metal is marked with white arrows in Fig. 9. The flow pattern at the rear region is strongly fluctuating and irregular. It is mainly driven by the momentum impact from the middle region, the capillary pressure and the Marangoni stress. The molten pool in the WFLBW has a similar shape with that in the autogenous LBW from other researchers' simulation works [39,40]. It is suggested that the adding of the filler material plays a minor role on the molten pool geometry, except for the reinforcement part, considering that only 7.2% of the laser energy is absorbed by the filler wire and the volume of filler material is less than 10% of the whole weld bead volume.
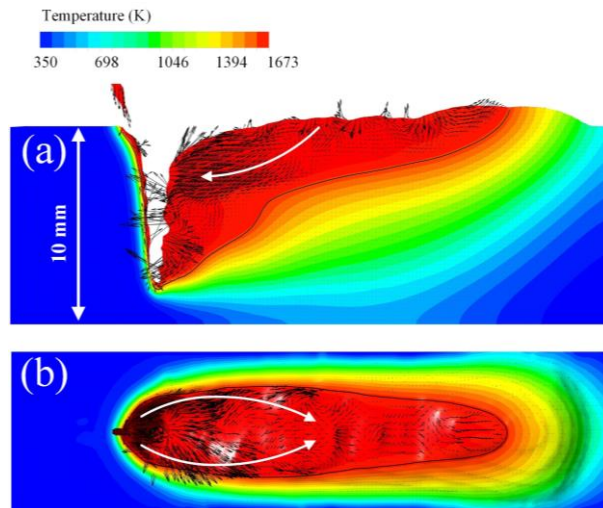
Fig. 9 Calculated temperature and velocity fields of WFLBW ($t = 0.875$ s): (a) x-z central plane, (b) top surface

Fig. 10 shows that the basic flow pattern remains similar after the EMS is applied. However, the melt flow along the x-z central plane changes from forward to downward as it approaches the rear wall of the keyhole, as shown in Fig. 10(a). Fig. 11 presents the comparison of velocity magnitude between WFLBW and EMS-WFLBW in the x-z central plane. For both processes, the peak velocity is located at the keyhole wall because the recoil pressure is the predominant driving force. In region I, there is no apparent influence on the velocity magnitude from the EMS. The effect of the Lorentz force is masked by the strong recoil pressure. The averaged velocity magnitude is increased from 0.08 m/s to 0.15 m/s in the rear part (region II), and from 0.04 m/s to 0.19 m/s in the lower part (region III).
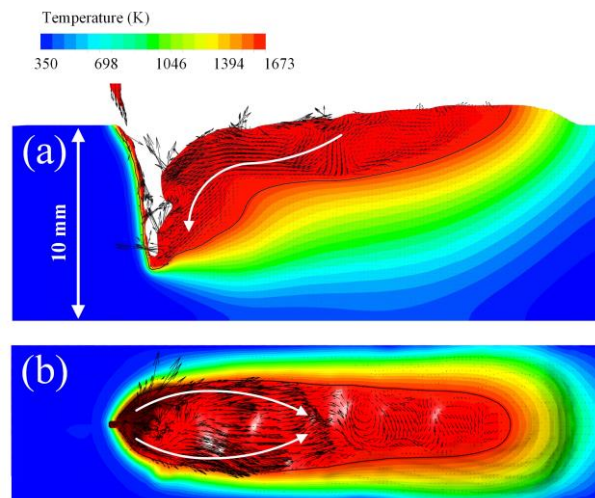
Fig. 10 Calculated temperature and velocity fields of EMS-WFLBW ($t = 0.875$ s): (a) x-z central plane, (b) top surface
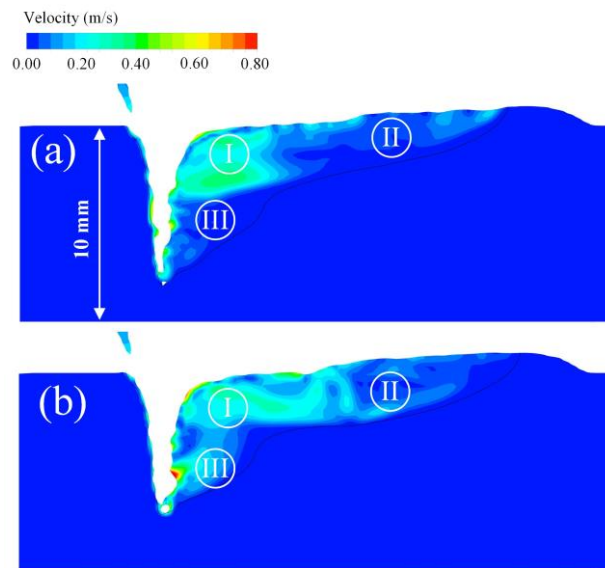

Fig. 11 Velocity magnitude at the x-z central plane: (a) WFLBW, (b) EMS-WFLBW

The EMS has a remarkable impact on the keyhole dynamics and the absorption of the laser energy is influenced. The numerical results show that the rear keyhole wall flows forward and contacts with the front keyhole wall, causing the collapse of the keyhole in both processes. More laser energy is absorbed at the collapse position to produce a stronger recoil pressure, and the keyhole is reopened. As a consequence, severe keyhole fluctuations can be observed, which agrees with X-ray transmission results [41]. A statistical analysis on the keyhole fluctuation is provided in Fig. 12. The amplitude of the keyhole fluctuation is the distance from the collapse position to the keyhole bottom. The probability distribution of the keyhole fluctuation amplitude obeys a normal distribution approximately for both cases. However, the keyhole collapses more frequently at the upper part under the EMS. 23% of the collapses occur at the upper part of the keyhole in the EMS-WFLBW, while it is only 13% in the WFLBW. As more upper keyhole collapses occur during the EMS-WFLBW, the downward transfer of the laser energy is blocked, reducing the penetration depth.
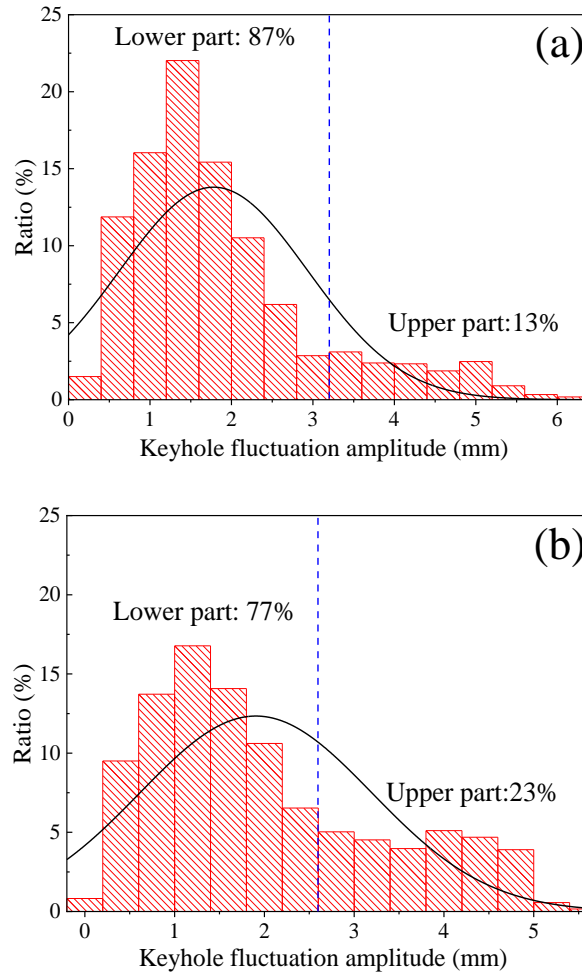
Fig. 12 Statistic results of keyhole fluctuation amplitude: (a) WFLBW, (b) EMS-WFLBW

4.3 Element transport behavior

The simulated Ni distribution in the resultant weld of the WFLBW is given in Fig. 13(a). The additional Ni from the filler material is distributed quite inhomogeneously and concentrates on the upper part of the weld. Once the oscillating magnetic field is applied, the Ni distribution is considerably homogenized by the EMS, as shown in Fig. 13(d). The experimentally measured Ni content from the EDX mapping shows a similar distribution with the calculated result. A more quantitative Ni distribution along the center line of the weld is plotted in Fig. 13(c) and (f), as well as the experimental data from the EDX line scanning with a higher resolution. The EDX data is averaged over a distance of 500 μm. Fig. 13(c) shows that the Ni distribution is relatively uniform at the upper part of the weld (about 40% of the whole penetration) in the WFLBW, and it decreases rapidly from 16% to the level of base metal in a transition region. The uniform region reaches around 70 % of the whole penetration depth with the EMS, and the transition region is narrowed from 2.7 mm to 1.0 mm,

as given in Fig. 10(f). The comparison between the calculated and the measured results shows a good agreement again.
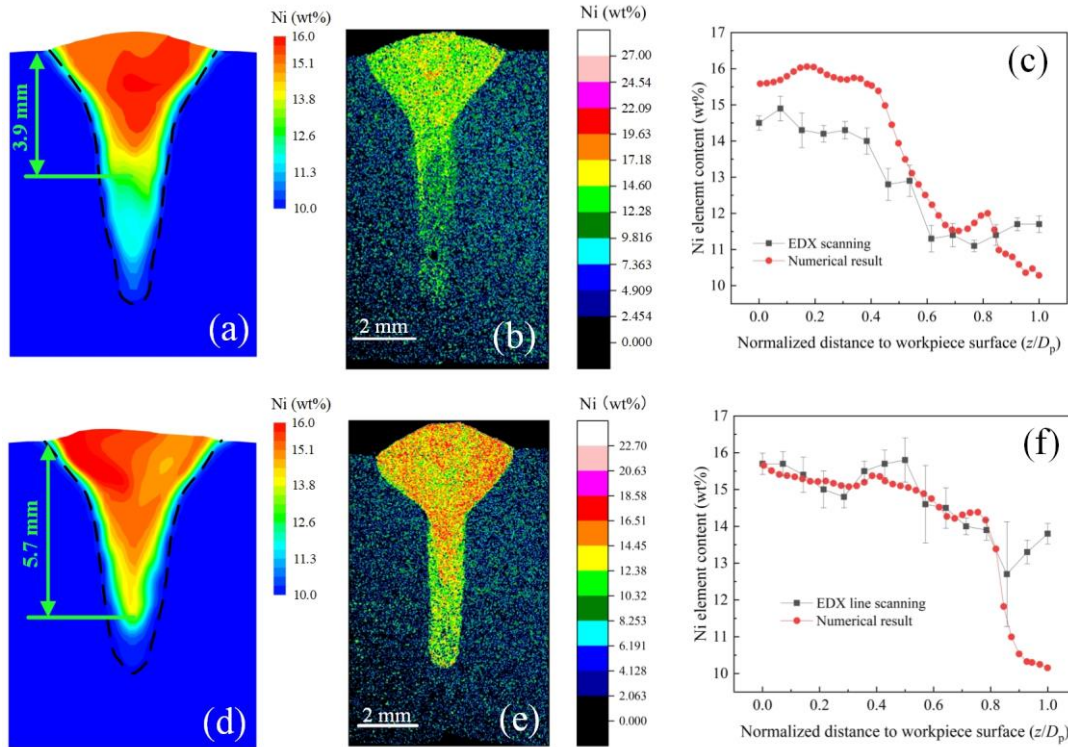

Fig. 13 Resultant Ni distribution in the cross-section: (a) and (c) from WFLBW, (d) and (f) from EMS-WFLBW

To obtain a clearer physical understanding of the beneficial effect from the EMS, the transport behavior of Ni in the molten pool is analyzed in detail. The ratio of advection to diffusion for Ni should be evaluated first by a dimensionless Peclet number (Pe).

$$Pe = \frac{D_p v_{max}}{2 D_{Ni}} \approx 1 \times 10^6 \quad (28)$$

where v_{max} is the maximum velocity in the molten pool and D_{Ni} is the Ni diffusion coefficient in iron. The extremely high value of the Peclet number indicates that the diffusion can be neglected, and the Ni distribution is dominated by the melt flow.

Fig. 14 gives the 3D distribution of the Ni content as well as the velocity field, i.e. the transport routine of Ni. The high-temperature filler material first impacts the upper part of the keyhole front wall. However, the melt flow on the keyhole front wall is quite irregular, as shown in Fig. 9(a). The additional material is not transferred along the front keyhole wall. Conversely, the filler material with higher Ni flows around the keyhole, and then backward along the lateral side of the molten pool.

Subsequently, the flowing direction changes at the middle part, and the liquid metal flows forward along the x-z central plane to bring the Ni to the forepart of molten pool. It should be noted that the forward flow along the x-z central plane is almost parallel to the welding direction, and the added Ni cannot be brought to the root of the weld.

As discussed above, the downward flow is enhanced by the EMS, which is evidently beneficial for the element homogeneity. The time-dependent velocity components in three directions at two positions (z = 7.5 mm and z = 6 mm at x-z central plane) are shown in Fig. 15. The velocity components are not influenced significantly by the EMS at the upper part of the molten pool, as suggested in Fig. 15 (a)-(c). The liquid metal has a high velocity component in the positive x direction, and the components in y and z directions fluctuate around zero in both processes. At the middle of the penetration depth (z=6 mm), the flow pattern is changed from backward to forward (typically -0.05 m/s vs. +0.05 m/s) and from upward to downward (typically +0.05 m/s vs. -0.10 m/s), as shown in Fig. 15 (d) and (f). It is indicated that the EMS promotes not only the downward flow but also the forward flow. Hence, the added Ni can be brought from the periphery to the central plane, and from the upper part to the root.

The filler material is further mixed at the rear region of the molten pool in the EMS-WFLBW since the melt flow is also accelerated there, as shown in Fig. 11. Although the penetration depth is stable after the quasi-steady state is reached, obvious spiking distribution of Ni exists at the root of fusion zone, as shown in Fig. 14(a). The spiking phenomenon is suppressed under the effect of the oscillating magnetic field.
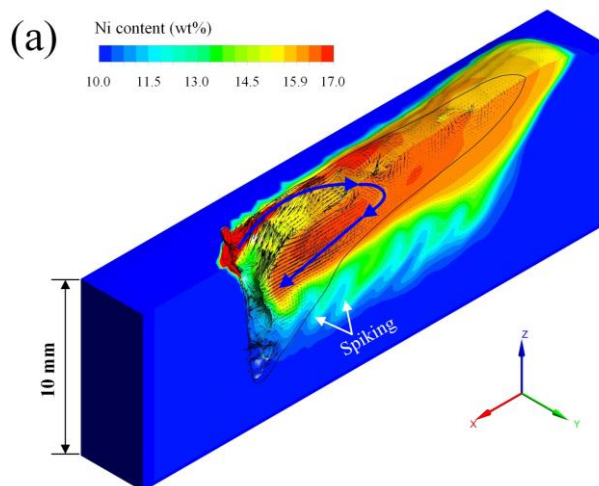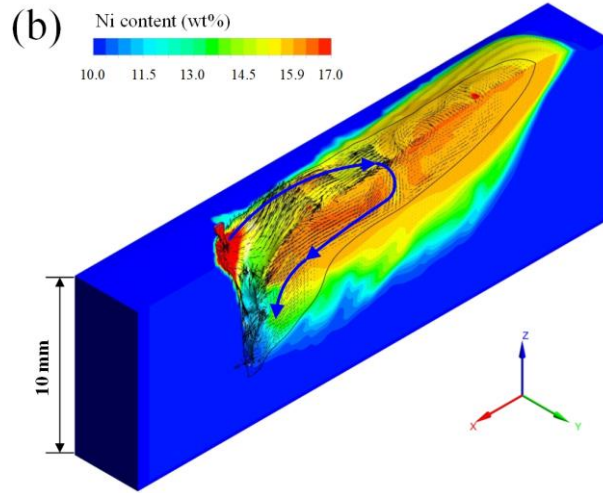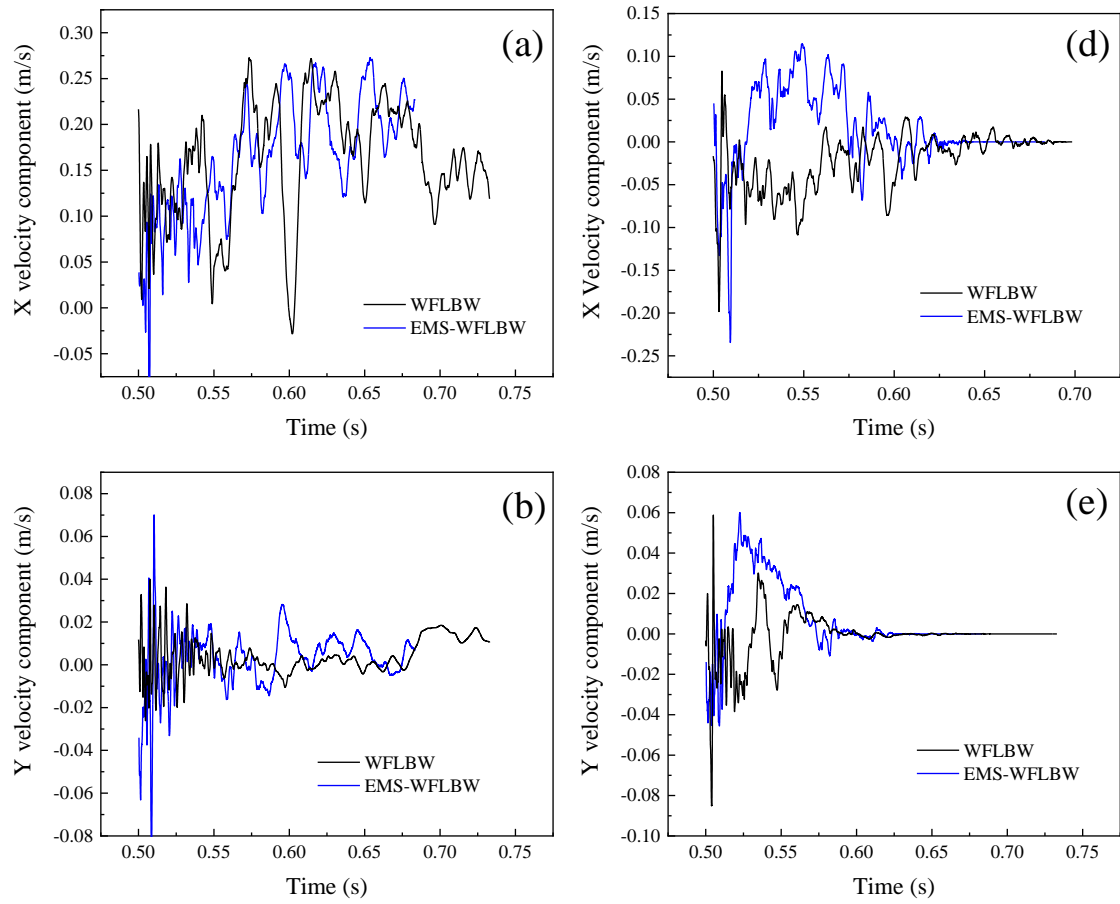
Fig. 14 3D transport routine of Ni in the molten pool: (a) WFLBW, (b) EMS-WFLBW.
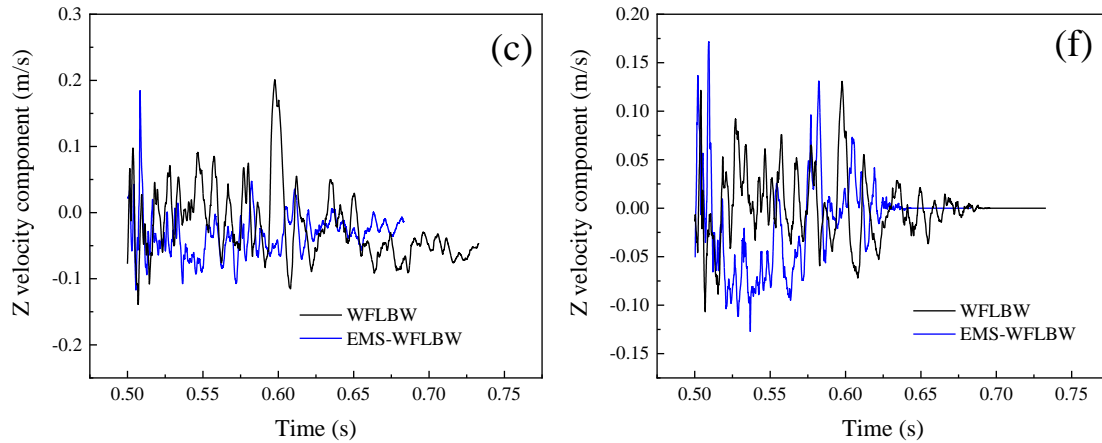
Fig. 15 Time-dependent velocity components in the x-z central plane: (a)-(c) at z = 7.5 mm, (d)-(f) at z = 6 mm.

5. Conclusions

An oscillating magnetic field is applied to produce electromagnetic stirring (EMS) in the molten pool of wire feed laser beam welding (WFLBW). The effect of the EMS on the thermo-fluid flow and the relevant element transport has been studied using multi-physical modelling and experimental methods. The following specific conclusions can be drawn:

(1) The induced eddy current can reach up to 1×10^7 A/m^2 under the magnetic field of 235 mT and 3600 Hz. Sufficient EMS can be produced in the molten pool by a Lorentz force with a maximum value of 1.9×10^6 N/m^3, which shows significant impacts on the heat and mass transfer behaviors.

(2) The melt flow velocity is increased by the EMS at the rear and lower regions of molten pool. The keyhole collapses more frequently at upper part under the stirring action.

(3) The added Ni from the filler material is distributed more homogeneously in the molten pool after the EMS is introduced, which can be predicted numerically by the model. The downward and forward flow along the x-z central plane is enhanced to bring Ni to the root of the weld in the EMS-WFLBW.

References

[1] M. Bachmann, A. Gumenyuk, M. Rethmeier, Welding with high-power lasers: trends and developments, Phys. Procedia 83 (2016) 15-25.

[2] M. J. Torkamany, A. F. Kaplan, F. M. Ghaini, M. Vänskä, A. Salminen, K. Fahlström, J. Hedegård, Wire deposition by a laser-induced boiling front, Opt. Laser Technol. 69 (2015) 104-112.

[3] D. Räbiger, Y. Zhang, V. Galindo, S. Franke, B. Willers, S. Eckert, The relevance of melt convection to grain refinement in Al–Si alloys solidified under the impact of electric currents, Acta Mater. 79 (2014) 327-338.

[4] N. S. Bondareva, M. A. Sheremet, M. A, Natural convection heat transfer combined with melting process in a cubical cavity under the effects of uniform inclined magnetic field and local heat source, Int. J. Heat Mass Transf. 108 (2017) 1057-1067.

[5] M. Kern, P. Berger, H. Huegel, Magneto-fluid dynamic control of seam quality in CO_2 laser beam welding. Weld. J. 79 (3) (2000), 72-78.

[6] X. Zhan, J. Zhou, W. Sun, J. Chen, Y. Wei, Effect of external applied steady magnetic field on the morphology of laser welding joint of 4-mm 2024 aluminum alloy, Appl. Phys. A 123 (1) (2017) 106.

[7] M. Bachmann, V. Avilov, A. Gumenyuk, M. Rethmeier, Experimental and numerical investigation of an electromagnetic weld pool control for laser beam welding, Phys. Procedia 56 (2014) 515-524.

[8] V. Avilov, A. Fritzsche, M. Bachmann, A. Gumenyuk, M. Rethmeier, Full penetration laser beam welding of thick duplex steel plates with electromagnetic weld pool support, J. Laser Appl. 28 (2) (2016) 022420.

[9] A. Fritzsche, K. Hilgenberg, F. Teichmann, H. Pries, K. Dilger, M. Rethmeier, Improved degassing in laser beam welding of aluminum die casting by an electromagnetic field, J. Mater. Process. Technol. 253 (2018) 51-56.

[10] M. Gatzen, Influence of low-frequency magnetic fields during laser beam welding of aluminium with filler wire, Phys. Procedia 39 (2012) 59-66.

[11] Y. Rong, J. Xu, H. Cao, H. Zheng, Y. Huang, G. Zhang, Influence of steady magnetic field on dynamic behavior mechanism in full penetration laser beam welding, J. Manu. Process. 26 (2017) 399-406.

[12] M. Gatzen, Z. Tang, F. Vollertsen, M. Mizutani, S. Katayama, X-ray investigation of melt flow behavior under magnetic stirring regime in laser beam welding of aluminum, J. Laser Appl. 23 (3) (2011) 032002.

[13] M. Bachmann, V. Avilov, A. Gumenyuk, M. Rethmeier, Numerical simulation of full-penetration laser beam welding of thick aluminium plates with inductive support, J. Phys. D-Appl. Phys. 45 (3) (2011) 035201.

[14] M. Bachmann, V. Avilov, A. Gumenyuk, M. Rethmeier, About the influence of a steady magnetic field on weld pool dynamics in partial penetration high power laser beam welding of thick aluminium parts, Int. J. Heat Mass Transf. 60 (2013) 309-321.

[15] M. Bachmann, V. Avilov, A. Gumenyuk, M. Rethmeier, Experimental and numerical investigation of an electromagnetic weld pool support system for high power laser beam welding of austenitic stainless steel, J. Mater. Process. Technol. 214 (2014) 578-591.

[16] M. Bachmann, V. Avilov, A. Gumenyuk, M. Rethmeier, Numerical assessment and experimental verification of the influence of the Hartmann effect in laser beam welding processes by steady magnetic fields, Int. J. Therm. Sci. 101 (2016) 24-34.

[17] M. Bachmann, R. Kunze, V. Avilov, M. Rethmeier, Finite element modeling of an alternating current electromagnetic weld pool support in full penetration laser beam welding of thick duplex stainless steel plates. J. Laser Appl. 28 (2) (2016), 022404.

[18] J. Chen, Y. Wei, X. Zhan, C. Gu, X. Zhao, Thermoelectric currents and thermoelectric-magnetic effects in full-penetration laser beam welding of aluminum alloy with magnetic field support, Int. J. Heat Mass Transf. 127 (2018) 332-344.

[19] M. Gatzen, Z. Tang, F. Vollertsen, Effect of electromagnetic stirring on the element distribution in laser beam welding of aluminium with filler wire, Phys. Procedia 12 (2011) 56-65.

[20] X. Chen, M. Luo, R. Hu, R. Li, L. Liang, S. Pang, Thermo-electromagnetic effect on weld microstructure in magnetically assisted laser welding of austenite steel, J. Manu. Process. 41 (2019) 111-118.

[21] C.S. Wu, Welding thermal Processes and weld Pool Behaviors, first ed., CRC Press/China Machine Press, Beijing, 2011.

[22] Y. Kawahito, N. Matsumoto, M. Mizutani, S. Katayama, Characterisation of plasma induced during high power fibre laser welding of stainless steel, Sci. Technol. Weld. Join. 13 (8) (2008), 744-748.

[23] V.R. Voller, C. Prakash, A fixed grid numerical modeling methodology for convection-diffusion mushy region phase change problems, Int. J. Heat Mass Transf. 30 (1987) 1709–1719.

[24] Y. Arata, H. Maruo, I. Miyamoto, R. Nishio. High Power CO_2 Laser Welding of Thick Plate: Multipass Weding with Filler Wire (Welding Physics, Process & Instrument), Transact JWRI 15 (2) (1986) 199-206

[25] W. Schulz, G. Simon, H. M. Urbassek, I. Decker, On laser fusion cutting of metals. J. Phys. D-Appl. Phys. 20 (4) (1987) 481-488.

[26] W. I. Cho, S. J. Na, C. Thomy, F. Vollertsen, Numerical simulation of molten pool dynamics in high power disk laser welding, J. Mater. Process. Technol. 212 (2012) 262-275.

[27] Y. Kawahito, N. Matsumoto, Y. Abe, S. Katayama, Relationship of laser absorption to keyhole behavior in high power fiber laser welding of stainless steel and aluminum alloy, J. Mater. Process. Technol. 211 (2011) 1563-1568.

[28] F. Lu, X. Li, Z. Li, X. Tang, H. Cui, Formation and influence mechanism of keyhole-induced porosity in deep-penetration laser welding based on three-dimensional transient modeling, Int. J. Heat Mass Transf. 90 (2015) 1143-1152.

[29] S. Muhammad, S. W. Han, S. J. Na, A. Gumenyuk, M. Rethmeier, Study on the role of recondensation flux in high power laser welding by computational fluid dynamics simulations, J. Laser Appl. 30 (1) (2018) 012013.

[30] V. Semak, A. Matsunawa, The role of recoil pressure in energy balance during laser materials processing. J. Phys. D-Appl. Phys. 30 (18) (1997) 2541.

[31] X. Meng, G. Qin, X. Bai, Z. Zou, Numerical analysis of undercut defect mechanism in high speed gas tungsten arc welding, J. Mater. Process. Technol. 236 (2016) 225-234.

[32] H. Ki, J. Mazumder, P. S. Mohanty, Modeling of laser keyhole welding: Part I. Mathematical modeling, numerical methodology, role of recoil pressure, multiple reflections, and free surface evolution, Metall. Mater. Transact. A 33 (6) (2002) 1817-1830.

[33] X. Meng, G. Qin, R. Zong, Thermal behavior and fluid flow during humping formation in high-speed full penetration gas tungsten arc welding, Int. J. Therm. Sci. 134 (2018) 380-391.

[34] Y. Su, Z. Li, K.C. Mills, Equation to estimate the surface tensions of stainless steels, J. Mater. Sci. 40 (9) (2005) 2201–2205.

[35] D. Peckner, I. Bernstein, Handbook of Stainless Steels, first ed., McGraw-Hill Book Company, New York, 1977.

[36] K. C. Mills, Recommended values of thermophysical properties for selected commercial alloys, first ed., Woodhead Publishing, Cambridge, 2002.

[37] K. D. Maglić, N. L. Perović, A. M. Stanimirović, Calorimetric and transport properties of Zircalloy 2, Zircalloy 4, and Inconel 625, Int. J. Thermophys. 15 (4) (1994) 741-755.

[38] Y. Ono, S. Matsumoto, Diffusion of chromium, manganese, and nickel in molten iron, Transact. Jpn. Inst. Met. 16 (7) (1975) 415-422.

[39] S. Y. Pang, W. D. Chen, W. Wang, A quantitative model of keyhole instability induced porosity in laser welding of titanium alloy, Metall. Mater. Transact. A 45 (6) (2014) 2808-2818.

[40] C. Panwisawas, B. Perumal, R. M. Ward, N. Turner, R. P. Turner, J. W. Brooks, H. C. Basoalto, Keyhole formation and thermal fluid flow-induced porosity during laser fusion welding in titanium alloys: Experimental and modelling, Acta Mater. 126 (2017) 251-263.

[41] Y. Kawahito, Y. Uemura, Y. Doi, M. Mizutani, K. Nishimoto, H. Kawakami, M. Tanaka, H. Fujii, K. Nakata, S. Katayama, Elucidation of the effect of welding speed on melt flows in high-brightness and high-power laser welding of stainless steel on basis of three-dimensional X-ray transmission in situ observation, Weld. Int. 31 (3) (2017) 206-213.